JOURNAL OF PROPULSION AND POWER
Vol. 12, No. 1, January–February 1996

Two-Fluid Nonequilibrium Simulation of Hydrogen Arcjet Thrusters

S. A. Miller* and M. Martinez-Sanchez†
Massachusetts Institute of Technology, Cambridge, Massachusetts 02139

A detailed numerical model has been developed to study the gasdynamic flow in an electrothermal arcjet thruster. This two-temperature Navier–Stokes model consistently incorporates viscosity, heat conduction, ohmic dissipation, collisional energy transfer between electrons and heavy species, ambipolar diffusion, nonequilibrium dissociation and ionization, and continuum radiation. The fluid equations are solved by MacCormack's method while an iterative procedure is used to relax an electric potential equation, from which the current distribution in the thruster is obtained. Using hydrogen propellant, solutions are achieved for a range of input parameters and the underlying physics and internal structures of these arcjet flows are revealed. In particular, a mechanism for self-sustaining anodic arc attachment is identified. Numerical solutions are compared with experimental results from the Stuttgart TT1 radiation-cooled arcjet thruster. Calculated discharge voltage is within 1–10% of experimental measurements, and predicted specific impulse is within 5–10% agreement. In addition, flow solutions are used to explain observed trends in performance as quantities such as the specific energy and mass flow rate are varied.

Nomenclature

$\hat{c}_v$ = specific heat at constant volume, J/mole K
D_a = ambipolar diffusion coefficient, m^2/s
$\boldsymbol{d}_e$ = ambipolar flux of ions and electrons, $m^{-2}\ s^{-1}$
E_d = dissociation energy, J
E_i = ionization energy, J
E_l = elastic collisional energy transfer, W/m^3
E_{vib} = vibrational excitation energy, J
$\boldsymbol{E}$ = electric field, V/m
e = electric charge, C; internal energy, J/kg
h = Planck's constant, J s; enthalpy, J/kg
I = total current, A
$\boldsymbol{j}$ = electric current density, A/m^2
K = equilibrium constant
k = Boltzmann's constant, J/K
m = particle mass, kg
$\hat{N}$ = Avogadro's number, $mole^{-1}$
n = number density, m^{-3}
$\dot{n}$ = net production rate, $m^{-3}\ s^{-1}$
p = scalar pressure, Pa
$\boldsymbol{q}$ = heat flux vector, W/m^2
R = real-gas constant, J/kg K
$\hat{R}$ = universal gas constant, J/mole K
$\dot{R}$ = energy loss due to radiation, W/m^3
T = temperature, K
$\boldsymbol{u}$ = mean flow velocity, m/s
$\boldsymbol{V}$ = slip velocity, m/s
v_B = Bohm velocity, m/s
x = mole fraction
α = ionization fraction
κ = coefficient of thermal conductivity, W/m K
μ = coefficient of viscosity, kg/m s
ν = collision frequency, s^{-1}
ρ = mass density, kg/m^3
σ = electrical conductivity, mho/m
$\langle \sigma v \rangle$ = reaction rate coefficient for $e - H_2$ dissociating collisions, m^3/s
Φ = viscous dissipation function, W/m^3
ϕ = electric potential, V
ψ = electron mobility, m^2/Ω C
Ω = average effective collision integral, m^2

I. Introduction

A SCHEMATIC diagram of an electrothermal arcjet is shown in Fig. 1. In this device an electric arc is passed between a central cathode and a surrounding anode. The anode effectively defines the geometry of the thruster constrictor and nozzle. The thermal energy of arc electrons is collisionally transferred to the flowing propellant and then converted to kinetic energy in the nozzle expansion to produce increased thrust. Low-power arcjet thrusters have recently been flight qualified through ground testing and are now being used in space for stationkeeping of geosynchronous communication satellites. Most of the impetus to date for design strategies, however, has come from empirical studies and experimentation and there is a need to better understand the underlying physics, detailed energy balances, and transport mechanisms of these devices.

Unfortunately, the complexity of the models and equations needed to accurately represent the flow in an arcjet thruster effectively limits the use of analytic techniques to simplified cases, through which one may obtain useful physical insights, but inadequate predictions of thruster performance. Experimental techniques provide much useful empirical data, but

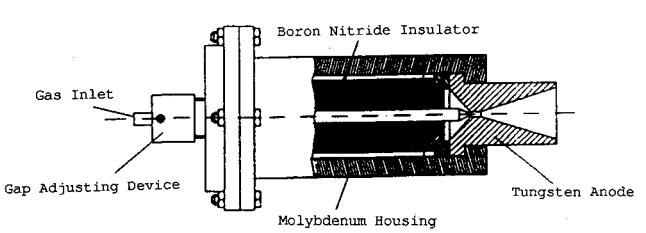

Fig. 1 Stuttgart 10-kW radiation-cooled arcjet thruster.

Presented as Paper 93-218 at the 23rd International Electric Propulsion Conference, Seattle, WA, Sept. 13–16, 1993; received Oct. 13, 1993; revision received April 14, 1995; accepted for publication May 9, 1995.

*Department of Aeronautics and Astronautics, Room 37-442, 77 Massachusetts Avenue; currently Senior Member, Technical Staff, The Aerospace Corporation, P.O. Box 92957, Los Angeles, CA 90009-2957.

†Professor, Department of Aeronautics and Astronautics, Room 37-401, 77 Massachusetts Avenue. Member AIAA.

many quantities of interest are not accessible in the important regions of the thruster. For these reasons numerical methods of solving the governing equations have become important tools for conducting arcjet research.

Previous numerical modeling of arcjet thrusters has focused on the development of one- and two-dimensional and axisymmetric models with relatively simple physics and geometries. The level of detail has ranged from one-dimensional models[1] to coupled quasianalytic models of the inner (arc) and outer (cold gas) flows,[2-4] to simplified axisymmetric space-marching techniques,[5] and finally to two-dimensional and axisymmetric viscous codes.[6-8] The latest research has obtained results that variously incorporate ohmic heating, electron heat conduction, dissociational and ionizational nonequilibrium, and empirical models of radiation losses. There are still a number of issues, such as viscous and diffusive effects, arc formation, and attachment, the heat balance in the anode, and ultimately the accurate prediction of voltage and efficiency, which need to be addressed. This article describes a generalized, more physically accurate model of the gasdynamic flow through an arcjet thruster, which includes the aforementioned effects with the exception of a coupled anode thermal analysis. The predictions of this model compare favorably to experimental results obtained with medium power hydrogen arcjets.

II. Model

A. Basic Assumptions

This model is based on an axisymmetric formulation. A component of the flow velocity in the azimuthal θ direction, however, is incorporated to account for the swirl injection of most experimental arcjets. Hydrogen was selected as the propellant of choice, due to its low molecular weight (and therefore high performance) and its simple molecular structure, which allows for analytic evaluation of the necessary transport coefficients. Nonequilibrium dissociation and ionization are modeled and four species of particles are tracked: diatomic molecules, monatomic neutrals and ions, and electrons. Dissociation is modeled by heavy species collisions and electron impact, and the ionization process is based on electron impact ionization and three-body recombination, with only H^+ ions considered.

The following assumptions are made regarding the state of the flow in the thruster and the physical processes involved. The plasma is assumed to be macroscopically neutral, so that $n_e = n_i$. Strong coupling is assumed between the ions and neutrals, designated together as the heavy species. This implies that $\boldsymbol{u}_i \cong \boldsymbol{u}_n \cong \boldsymbol{u}$ (except for ambipolar diffusion), and $T_i \cong T_n \cong T_g$. Self-consistently incorporated effects include ambipolar diffusion, heat conduction, viscous shear and dissipation, ohmic heating, collisional energy transfer between electrons and heavy species, and energy lost through continuum radiation. Line radiation is neglected since the escape coefficients are extremely small for this case.[9] The self-induced magnetic field in the ionized gas is neglected due to the low current density in the thruster,[9] and the individual species are assumed to obey the ideal gas law. Given the aforementioned assumptions, the model can be summarized by a set of nine partial differential equations that must be solved locally in order to generate a viable simulation of the flow.

B. Governing Equations

The equations that govern the model arcjet thruster of this research are essentially a group of modified Navier–Stokes equations. These include an equation of state and equations for the ion, neutral atom, and global density; the axial, radial, and azimuthal global momentum; the electron and heavy species energy; and the electric potential. To maintain numerical robustness, these equations are written in conservative form. Source terms that cannot be expressed in flux vector form are included as necessary.

The electric potential equation is derived by combining Ohm's law $\boldsymbol{j} = \sigma\boldsymbol{E} + \psi\nabla p_e$ with the equation $\nabla\cdot\boldsymbol{j} = 0$, where $\psi = e/m_e \Sigma_r \nu_{er}$ is the electron mobility. Assuming a potential of the form $\boldsymbol{E} = -\nabla\phi$, the resulting equation is given by

$$\frac{1}{r}\frac{\partial}{\partial r}\left(r\sigma\frac{\partial\phi}{\partial r}\right) + \frac{\partial}{\partial z}\left(\sigma\frac{\partial\phi}{\partial z}\right) = \psi\left(\frac{\partial^2 p_e}{\partial r^2} + \frac{1}{r}\frac{\partial p_e}{\partial r} + \frac{\partial^2 p_e}{\partial z^2}\right) + \frac{\partial p_e}{\partial r}\frac{\partial\psi}{\partial r} + \frac{\partial p_e}{\partial z}\frac{\partial\psi}{\partial z} \tag{1}$$

The global density equation is obtained by summing the individual species continuity equations:

$$\frac{\partial\rho r}{\partial t} + \frac{\partial\rho u_r r}{\partial r} + \frac{\partial\rho u_z r}{\partial z} = 0 \tag{2}$$

For the ion (or electron) density, the governing equation is derived from the statement of ion mass conservation, modified to account for the ambipolar flux of charged particles in terms of ion density gradients:

$$\frac{\partial\rho_e r}{\partial t} + \frac{\partial(\rho_e u_r + d_{er})r}{\partial r} + \frac{\partial(\rho_e u_z + d_{ez})r}{\partial z} = m_e\dot{n}_e r \tag{3}$$

where $\boldsymbol{d}_e$ is given by[9]

$$\boldsymbol{d}_e = -D_a\nabla\rho_e, \qquad D_a = \sqrt{\frac{\pi k T_g}{4m_n}}\frac{[1 + (T_e/T_g)]}{Q_{in}(n_e + n_n)} \tag{4}$$

In the source term, $\dot{n}_e$ represents the net rate of production of ions per unit volume through inelastic collisional processes. The statement of atomic hydrogen mass conservation is obtained in a similar manner and the effect of ambipolar diffusion is consistently included by assuming that both neutral species travel at the same velocity:

$$\frac{\partial\rho_H r}{\partial t} + \frac{\partial\rho_H u_r r}{\partial r} - \frac{\partial}{\partial r}\left[\frac{\rho_H}{(\rho_{H_2} + \rho_H)}\frac{m_H}{m_e}d_{er}r\right] + \frac{\partial\rho_H u_z r}{\partial z} - \frac{\partial}{\partial z}\left[\frac{\rho_H}{(\rho_{H_2} + \rho_H)}\frac{m_H}{m_e}d_{ez}r\right] = m_H(\dot{n}_H + \langle\sigma v\rangle n_e n_{H_2} - \dot{n}_e)r \tag{5}$$

In this equation the source term represents the net rate of production of neutral atoms, given by the difference between the net rate of production due to dissociation and the net rate of ionization of those neutral atoms produced.

The three global momentum equations are

$$\frac{\partial\rho u_r r}{\partial t} + \frac{\partial(\rho u_r^2 + p - \tau_{rr})r}{\partial r} + \frac{\partial(\rho u_r u_z - \tau_{rz})r}{\partial z} + \tau_{\theta\theta} - \rho u_\theta^2 - p = 0 \tag{6}$$

$$\frac{\partial\rho u_\theta r}{\partial t} + \frac{\partial(\rho u_r u_\theta - \tau_{r\theta})r}{\partial r} + \frac{\partial(\rho u_\theta u_z - \tau_{\theta z})r}{\partial z} + \rho u_r u_\theta = 0 \tag{7}$$

$$\frac{\partial\rho u_z r}{\partial t} + \frac{\partial(\rho u_r u_z - \tau_{rz})r}{\partial r} + \frac{\partial(\rho u_z^2 + p - \tau_{zz})r}{\partial z} = 0 \tag{8}$$

where the corresponding τ_{ij} are the viscous stress tensor components.

The heavy species energy equation is

$$\frac{\partial \rho e_g r}{\partial t} + \frac{\partial(\rho e_g u_r + q_{gr})r}{\partial r} + \frac{\partial(\rho e_g u_z + q_{gz})r}{\partial z} + \frac{\partial(\rho_{H_2} e_{H_2} V_{H_2 r} + \rho_H e_H V_{Hr} + \rho_{H^+} e_{H^+} V_{H^+ r})r}{\partial r} + p_{H_2}\frac{\partial V_{H_2 r} r}{\partial r} + p_H \frac{\partial V_{Hr} r}{\partial r} + p_{H^+}\frac{\partial V_{H^+ r} r}{\partial r} + p_g\left(\frac{\partial u_r r}{\partial r} + \frac{\partial u_z r}{\partial z}\right) = \left(\Phi + E_l - \frac{1}{2}E_d \dot{n}_H\right) r \quad (9)$$

where the internal energy and enthalpy are defined by

$$\rho e_g = \frac{3}{2}(\rho_H + \rho_{H^+})R_H T_g + \frac{5}{2}\rho_{H_2} R_{H_2} T_g + \frac{\rho_{H_2} R_{H_2}\theta_v}{\exp(\theta_v/T_g) - 1} - \frac{7}{4}\rho R_H T_f \quad (10)$$

$$\rho h_g = \rho e_g + \rho_{H_2} R_{H_2} T_g + (\rho_H + \rho_{H^+})R_H T_g \quad (11)$$

Here, T_f is the reference temperature at which the enthalpy of molecular hydrogen is zero. Additional flux terms have been included in the heavy species energy equation to account for the radial transport of energy by ambipolar diffusion. Also, in Eq. (9), $q_g = -\kappa_g \nabla T_g$ is the heat flux vector and

$$E_l = 3(\rho_e/m_H)(\nu_{eH^+} + \nu_{eH} + \delta_s \nu_{eH_2})k(T_e - T_g) \quad (12)$$

represents the collisional energy transfer between electrons and heavy species. The coefficient δ_s in Eq. (12) is necessary to correct for the fact that electron–H_2 collisions are inelastic in nature. The magnitude of δ_s as a function of electron temperature is taken from Sutton and Sherman.[10]

For electrons, the governing energy equation is

$$\frac{\partial \rho_e E_e r}{\partial t} + \frac{\partial(\rho_e u_{er} H_e + q_{er})r}{\partial r} + \frac{\partial(\rho_e u_{ez} H_e + q_{ez})r}{\partial z} = \left(\frac{j^2}{\sigma} - E_l - E_d\langle\sigma v\rangle n_e n_{H_2} - E_i \dot{n}_e - \dot{R}\right) r \quad (13)$$

Here, j^2/σ represents heating due to ohmic dissipation, and the total energy and enthalpy are given by

$$E_e = \tfrac{3}{2}R_e T_e + \tfrac{1}{2}u_e^2 \quad \text{and} \quad H_e = E_e + R_e T_e \quad (14)$$

The final equation required for closure of the set is the equation of state:

$$p = \sum_j p_j = \sum_j n_{gj} k T_g + n_e k T_e \quad (15)$$

C. Dissociation and Ionization

The nonequilibrium dissociation rate $\dot{n}_H$ is derived by following the procedure and nomenclature of Biasca[11] for collisions of heavy species. Accordingly, this rate is given by

$$\dot{n}_H = A\hat{N}T_g^n \exp\left(-\frac{B}{\hat{R}T_g}\right)(\hat{m}_H \sigma_H + \hat{m}_{H_2}\sigma_{H_2}) \times \left[\sigma_{H_2} - \frac{\hat{R}T_g}{K_p(T_g)}\sigma_H^2\right] \quad (16)$$

where K_p is the equilibrium constant in terms of partial pressures, σ_j are the species molar concentrations, and the appropriate constants for hydrogen are taken from Rogers and Schexnayder.[12] Dissociation by $e - H_2$ collisions is represented by the second term on the right-hand side of Eq. (5), where $\langle\sigma v\rangle$ as a function of electron temperature is taken from Janev et al.[13] For ionization, the finite production rate is given by the generalized model of ionization and three-body recombination,[14] modified by Sheppard[15] to include a more accurate recombination coefficient based on a 19-level model of the dynamic equilibrium between excited states of the hydrogen atom:

$$\dot{n}_e = R n_e(S n_H - n_e^2) \quad (17)$$

$$S = \left(\frac{2\pi m_e k T_e}{h^2}\right)^{3/2} \exp(-E_i/kT_e) \quad (18)$$

$$R = 6.985 \times 10^{-42} \exp\left\{\frac{[f_r(T_e/1000) - 4.0833]^2}{0.8179}\right\} \quad (19)$$

D. Transport Properties

Because of the multicomponent nature of the gas in an electrothermal arcjet, the equations for the transport properties become quite complex. Since data are more readily available for hydrogen in the form of collision integrals, a formulation of the transport coefficients based on these integrals rather than on collision cross sections is implemented. As an example of the form of the transport coefficients used in this model, the gas coefficient of viscosity is given by Eq. (20). It is calculated based on a mean free path mixture formula, which is a function of the collision integrals and the species number densities and pure viscosities[14]:

$$\mu_g = \frac{n_{H_2}\mu_{H_2}}{n_{H_2} + n_H\sqrt{\frac{2}{3}}[\bar{\Omega}^{(2,2)}_{H_2-H}/\bar{\Omega}^{(2,2)}_{H_2-H_2}]} + \frac{n_H\mu_H}{n_H + n_{H_2}\sqrt{\frac{4}{3}}[\bar{\Omega}^{(2,2)}_{H_2-H}/\bar{\Omega}^{(2,2)}_{H-H}] + 2n_H + [\bar{\Omega}^{(2,2)}_{H-H^+}/\bar{\Omega}^{(2,2)}_{H-H}]} + \frac{n_{H^+}\mu_{H^+}}{n_{H^+} + 2n_H[\bar{\Omega}^{(2,2)}_{H-H^+}/\bar{\Omega}^{(2,2)}_{H^+-H^+}]} \quad (20)$$

Pure viscosities are given to lowest order by

$$\mu_j = 2.6693 \times 10^{-26}\frac{(M_j T_g)^{1/2}}{\bar{\Omega}^{(2,2)}_{jj}} \quad (21)$$

Electron and heavy species thermal conductivity coefficients are calculated based on similar mean free path arguments and mixture rules, and the electrical conductivity is taken from a first-order approximation by Grier.[16] Collision integrals required in the calculation of transport coefficients are interpolated as a function of temperature from data by Grier,[16] Belov,[17] and Vanderslice et al.[18] The accuracy of the previous approximate formulas for the transport coefficients was verified by comparison to previous, more detailed work for hydrogen in thermal and ionizational equilibrium.[16–19]

III. Numerical Method

A. Integration Scheme

The governing fluid equations are numerically integrated using MacCormack's explicit node-based method, which is second-order accurate in time and space. An empirical stability formula developed by MacCormack and Baldwin[20] is used to calculate the integration time step, which is then multiplied by a fractional coefficient to account for the effect of source terms and nonlinearities. Although MacCormack's method contains some inherent dissipation, additional second- and fourth-order smoothing terms are required to damp

unwanted numerical oscillations in the fluid equations. The electric potential equation, being predominantly elliptic in nature, is solved by iteration using a successive overrelaxation technique. Since the physical grid is nonuniform in order to closely represent the geometry of the actual arcjet being modeled, the governing equations are transformed into natural coordinates. A 150 by 30 point mesh is used, with grid concentrations near the walls, in the constrictor, and near the cathode tip in order to resolve the steep gradients associated with these regions.

B. Boundary Conditions

The conditions at the inlet of the computational domain, located 1 cm upstream of the cathode tip, are taken to be those of a subsonic uniform flow. A fraction of the total inlet velocity is specified as being in the azimuthal direction in order to simulate an injected swirl. The mass flow rate and total enthalpy are specified based on the particular run parameters, and the ionization fraction is set to a small but finite value, e.g., 10^{-7}. The density is obtained from a downwind finite difference approximation of the overall continuity equation and the inlet electron temperature is set equal to that of the next inside point. Finally, no current is allowed to pass upstream of the cathode tip.

The boundary conditions at the outlet of the thruster depend on whether the exit flow is subsonic or supersonic. In both cases the electron temperature is set equal to that of the next inside point and no current is allowed to pass beyond the exit plane. If the flow is supersonic at a point on the exit plane then the remaining variables are extrapolated from their values at the preceding two grid points of the mesh. If the flow is subsonic then the exit pressure is set equal to a small value representing near-vacuum conditions and the remaining variables are given by Riemann invariants with no electric or transport effects included.

For those boundary points lying beyond the tip of the cathode on the centerline, the radial and azimuthal flow velocities are set equal to zero and a zero radial gradient is imposed on the other variables.

Flow boundary conditions at the thruster walls include viscous no-slip conditions for the heavy species velocities and an imposed zero gradient on the electron temperature. The heavy species temperature is held constant at 1000 K upstream of the constrictor, increasing linearly to 1100 K at the constrictor exit. This profile was chosen based on experimental and numerical calculations of the anode wall temperature distribution for a reasonable operating range of the German TT1 radiatively cooled arcjet thruster.[9,21] On the cathode the wall temperature is allowed to increase to a maximum of 2000 K at the tip. For the boundary condition on electron density at each electrode, a balance is postulated between the flux of ions arriving at the sheath edge by ambipolar diffusion and the flux of ions arriving at the wall by virtue of their thermal energy at v_B:

$$D_a \frac{dn_e}{dy} = 0.61 n_e v_B, \qquad v_B = \sqrt{\frac{k(T_e + T_g)}{m_g}} \tag{22}$$

Application of the perpendicular overall momentum equation at the walls provides the approximate condition

$$\left.\frac{dp}{d\hat{n}}\right|_{\text{wall}} = 0$$

The boundary conditions on the wall electric potential are 1) that there is no current perpendicular to an insulating section and 2) that the potential on the anode is set equal to a fixed voltage that is the same for all simulated cases. For numerical reasons, anode current attachment is restricted to that portion of the outer wall downstream of the constrictor exit. It was found that when this restriction is removed, the model predicts attachment near the constrictor inlet, which is not borne out by experiment for the thruster studied. Some simplifications are made in order to avoid detailed modeling of the complex sheath physics of each electrode. On the cathode tip, a uniform axial current density is prescribed that sums to the specified total current. The potential at the cathode is then chosen to maintain this current level. A cathode voltage drop equal to the ionization potential plus one-half of the dissociation potential of the gas is added to the calculated voltage in order to account for the model's neglect of the cathode sheath region. In addition, an anode voltage drop is subtracted from the calculated voltage in order to account for the anode sheath region. A negative potential gradient is required in this sheath to turn back excess electrons, since the extracted current is much less than the random thermal flux of electrons to the anode wall ($j_{\text{anode}} << \frac{1}{4} e n_e \bar{c}_e$). This voltage drop is given by[9]

$$\Delta V_a = \frac{kT_e}{e}\left[\ln\left(\frac{\sqrt{m_i/m_e}}{0.61\sqrt{2\pi}}\right) - \ln\left(1 + \frac{j}{0.61 e n_e \sqrt{kT_e/m_i}}\right)\right] \tag{23}$$

IV. Results

A. Baseline Case

Results have been achieved for comparison to the Stuttgart TT1 radiation-cooled arcjet thruster[21] at a number of operating points. This thruster has a constrictor diameter and length of 2.5 and 5 mm, respectively, a nozzle half-angle of 17.5 deg, and an exit diameter of 25 mm. A baseline case of $\dot{m} = 0.1$ g/s and $I = 100$ A has been selected to show detailed flow results. Table 1 compares bulk results of the simulation to experimental measurements for this case, while Figs. 2–12 show line and contour plots of representative quantities. There is excellent agreement in the voltage between predicted and experimental results and good agreement (within 7%) in the thrust and specific impulse. The accuracy in voltage prediction shows that the simulation is accurately modeling electrical conductivity, arc growth, and current attachment given the assumptions that have been made regarding current at-

Table 1 Comparison of predicted and experimental results for the baseline case

	Predicted	Experiment
Voltage, V	115	112
Power, kW	11.5	11.2
Thrust, N	1.01	0.94
Specific impulse, s	1030	960
Efficiency	0.442	0.395

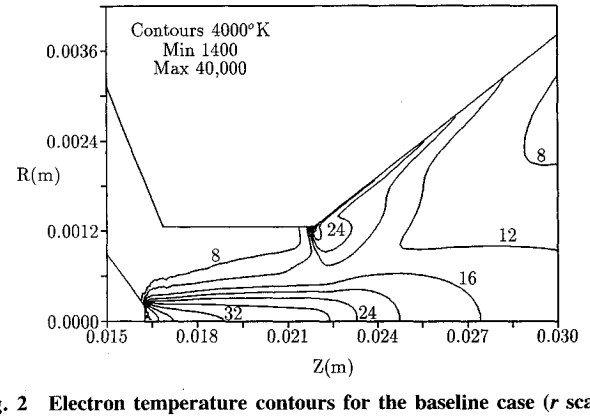

Fig. 2 Electron temperature contours for the baseline case (*r* scale exaggerated).

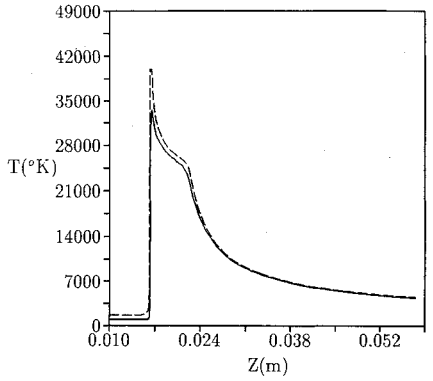

Fig. 3 Centerline axial profiles of gas and electron temperatures for the baseline case. ——, gas temperature; – – –, electron temperature.

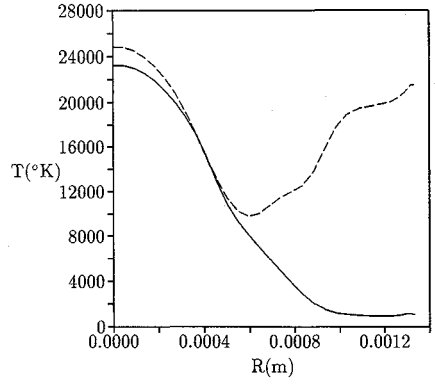

Fig. 4 Radial profiles of electron and heavy species temperatures 0.25 mm downstream of the constrictor exit. ——, gas temperature; – – – electron temperature.

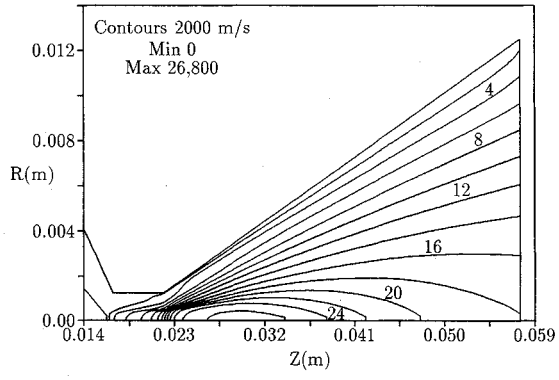

Fig. 5 Axial velocity contours for the baseline case (*r* scale exaggerated).

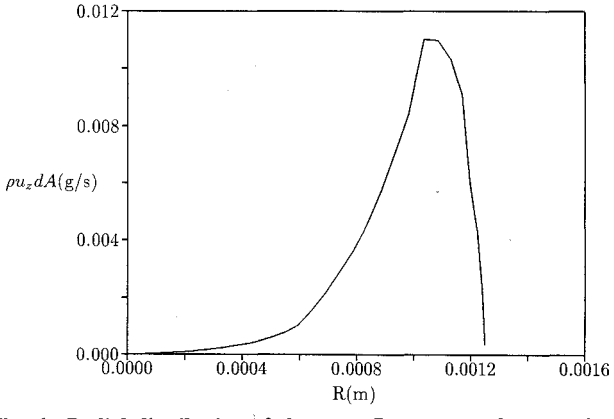

Fig. 6 Radial distribution of the mass flow rate at the constrictor exit for the baseline case.

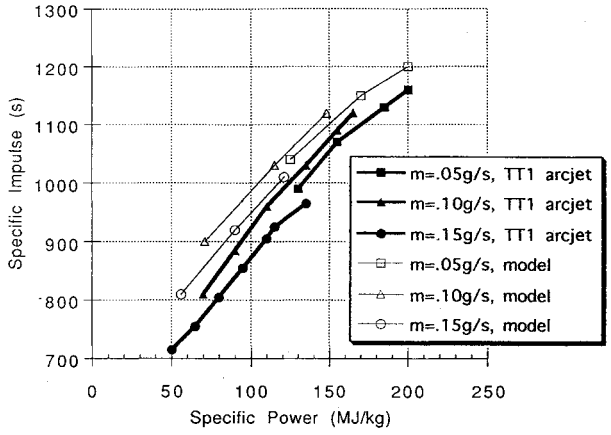

Fig. 7 Predicted I_{sp} compared to experimental data, German TT1 radiation-cooled hydrogen arcjet.

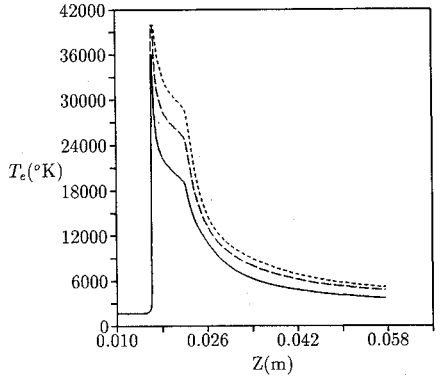

Fig. 8 Centerline axial electron temperature profiles for $\dot{m}$ = 0.1 g/s at three applied currents. ——, I = 60 A; – – –, I = 100 A; ----, I = 130 A.

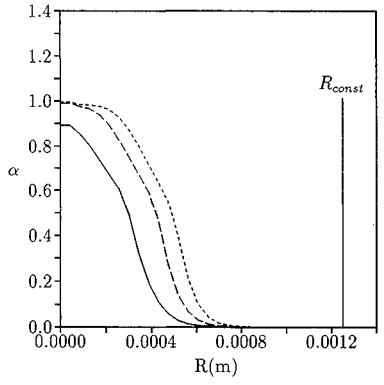

Fig. 9 Ionization fraction radial profiles at the constrictor exit for $\dot{m}$ = 0.1 g/s at three applied currents. ——, I = 60 A; – – –, I = 100 A; ----, I = 130 A.

tachment in the constrictor and electrode sheath voltage drops. The overprediction of thrust may be a result of inaccurately specified boundary conditions for the electrode temperatures and the inlet gas temperature, or it may reflect remaining deficiencies in modeling the anodic arc attachment region.

The simulated discharge voltage includes a bulk voltage drop from the electric arc and near-electrode voltage drops at the cathode tip and the anode wall. The near-cathode voltage drop ΔV_c is composed of a 15.8-V drop assigned to the cathode sheath ($V_i + \frac{1}{2}V_d$) and an 8-V drop calculated in the first few grid points downstream of the tip. $\Delta V_a \approx 15$ V is composed of a 22-V drop captured by the simulation and a −7-V drop associated with the electron-repelling sheath. The anode voltage drop is associated with the net deposition of

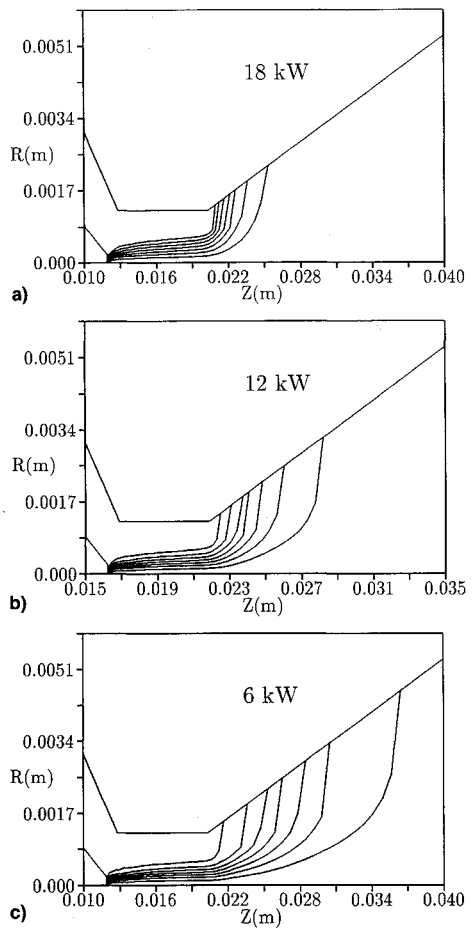

Fig. 10 Enclosed current contours for $P/\dot{m}$ = 120 MJ/kg: a) I = 60 A, $\dot{m}$ = 0.05 g/s; b) I = 100 A, $\dot{m}$ = 0.10 g/s; and c) I = 130 A, $\dot{m}$ = 0.15 g/s (bottom); (r scale exaggerated).

energy into the anode block by heavy species heat conduction and by the impingement of current-carrying electrons. Assuming that the energy transferred per unit area is of the form

$$j_a \Delta V_a = -k_g \frac{dT_g}{d\hat{n}} + u_{e\hat{n}} \left(\frac{5}{2} p_e + \frac{1}{2} \rho_e u_e^2 + E_i n_e \right) \quad (24)$$

using the results of the baseline flow simulation yields an equivalent voltage of 14.5 V for this deposited power, which agrees well with the ΔV_a seen in the potential profile.

Enclosed current contours for the baseline case are plotted in Fig. 10b. In this case, the bulk of the current attaches within the first quarter of the nozzle, peaking just downstream of the constrictor exit. Note that this figure graphs enclosed current contours in an approximate sense; plots of current streamlines show that the current does in fact attach perpendicular to the anode wall, which is not apparent in Fig. 10.[9] The flow becomes fully ionized along the centerline immediately downstream of the cathode tip and remains so through the first part of the nozzle expansion, beyond which there is some recombination. The boundary of the partially ionized region grows to approximately 50% of the channel by the constrictor exit and this region is essentially entrained in the flow throughout the nozzle. The primary heating mechanism is ohmic dissipation, which peaks locally on the thruster axis in the constrictor and just beyond the constrictor exit near the anode wall. This is evidenced by the local maxima in electron temperature in these regions (Fig. 2).

Within the highly ionized region of the arc in the constrictor, collisional energy transfer between electrons and heavy species raises the gas temperature to 20,000–30,000 K, or

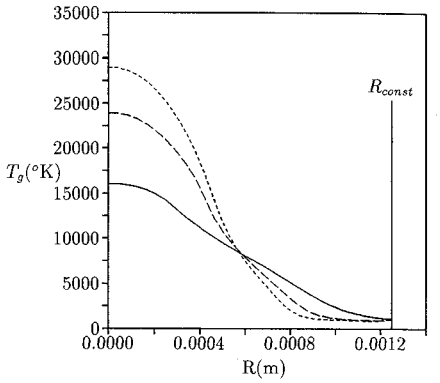

Fig. 11 Gas temperature radial profiles at the constrictor exit for $P/\dot{m}$ = 120 MJ/kg at three mass flow rates. ——, $\dot{m}$ = 0.05 g/s; – – –, $\dot{m}$ = 0.10 g/s; ----, $\dot{m}$ = 0.15 g/s.

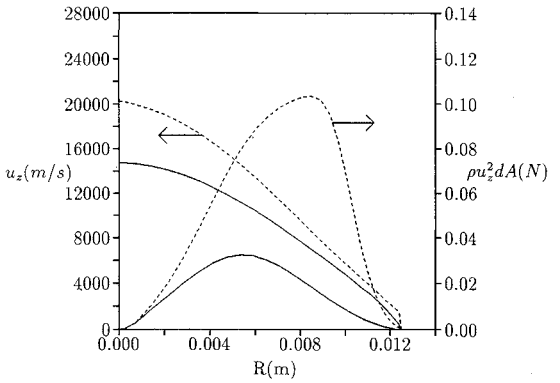

Fig. 12 Axial velocity and kinetic thrust radial profiles at the thruster exit for $P/\dot{m}$ = 120 MJ/kg at two mass flow rates. ——, $\dot{m}$ = 0.05 g/s; ----, $\dot{m}$ = 0.15 g/s.

nearly the same temperature as the electrons (Fig. 3). Because of the very low ionization fraction outside of the arc, however, the gas temperature in the outer flow remains approximately equal to that of the anode wall (Fig. 4). The calculated electron temperature at the thruster exit varies from 2000–4000 K, which compares favorably with measurements made by Hoskins et al.[22] on similar radiation-cooled hydrogen arcjets.

Since the pressure is nearly uniform over the cross section, rapid acceleration of the core flow occurs throughout the high-temperature, low-density region of the arc in the constrictor. Once the bulk of the pressure work has been done in the expansion process, however, viscous forces arising from steep velocity gradients in the central core decelerate the flow significantly in the nozzle expansion (Fig. 5). Both the inner and the outer flows accelerate smoothly through sonic velocity at the constrictor exit and a peak Mach number of 2.86 is reached at the thruster exit approximately halfway between the thruster axis and the anode wall.

The mass flow diagram of Fig. 6 points out an interesting description of how an arcjet works. This plot of the integrated mass flux at the constrictor exit shows that most of the mass actually flows outside of the high-temperature, high-velocity arc core. According to the model, the effect of the central arc is to produce an electrothermal, or fluid dynamic, plug, which forces most of the mass flow outward into the relatively low-temperature region near the anode wall. This process effectively decreases the throat area, thereby increasing the stagnation pressure of the plenum and increasing the thrust of the device. This is not the full explanation, however, because there is considerable heating of that fraction of the propellant that flows in the core region of the arc. This core fraction additionally transfers a portion of its energy to the outer flow by diffusion in the nozzle.

The effectiveness of this model in simulating the current attachment region at the anode is due to the incorporation of separate energy equations for heavy species and electrons and to the use of finite rate dissociation and ionization equations. Ohmic dissipation is found to be an important source of energy throughout the current path shown in Fig. 10, both inside and outside the main arc core. This leads to electron temperatures as high as 20,000 K in the anode attachment zone of the outer flow (Fig. 2), much higher than the 1000–2000 K temperatures that would be calculated by a model with only one energy equation. These elevated electron temperatures produce enough electron impact dissociation and ionization to create the necessary charge carriers for electrical conduction between the outer arc boundary and the anode. Ambipolar diffusion also plays a role in moving ions and electrons outward from the arc into the surrounding cooler gas flow.

To gain an understanding of the loss mechanisms involved in this particular arcjet thruster design, the partition of energy in the flow at the exit plane can be examined. By conservation of energy, the total power in the exiting flow is equal to the electrical input power minus the power lost to the walls plus the power inherent in the inlet flow, for a total of 14.6 kW for the baseline case. The power lost due to continuum radiation is found to be negligible for this thruster.[9] Table 2 catalogs the distribution of power in the various energy states of the exiting flow. As the table shows, in this case only 39% of the exit plane energy is in the form of useful thrust. Fully 47% of the energy is tied up in dissociation and ionization, while 13% is classified as thermal energy. In particular, the energy bound in dissociation and ionization represents a significant frozen loss.

B. Performance Mapping

A number of cases have been run to evaluate the model's effectiveness in predicting arcjet performance over a range of parameters. Figure 7 shows simulation predictions of specific impulse for the TT1 thruster at three mass flow rates and over a range of applied currents. The simulated specific impulse is seen to be approximately 5–10% higher than that measured by experiment. Voltage predictions from the arcjet simulation, listed in Table 3, fall within 1–3% of experiment for $\dot{m}$ = 0.05 and 0.1 g/s and within 10–12% for $\dot{m}$ = 0.15 g/s. The negative slope of the V–I relationship is also captured. The differences in predictive voltage accuracy between mass flow rates probably result from the boundary condition that requires the current to attach downstream of the constrictor exit. In reality this attachment point is a function of the operating conditions and may also be affected by sheath layers or instabilities not addressed by this research.

Table 2 Distribution of energy in the exit flow[a]

Energy state	Power, W	% of total
Axial kinetic	5720	39.2
Radial kinetic	89	0.6
Azimuthal kinetic	<1	0.0
Ionization	2546	17.5
Dissociation	4367	30.0
Electron thermal	88	0.6
Heavy species thermal	1769	12.1

[a]TT1 arcjet, I = 100 A, $\dot{m}$ = 0.1 g/s.

Table 3 Comparison of discharge voltages for the cases in Fig. 9

Case		Voltage	
I, A	$\dot{m}$, g/s	Numerical	Experiment
70	0.05	89	86
100	0.05	85	78
60	0.10	118	117
100	0.10	115	112
130	0.10	113	111
60	0.15	140	127
95	0.15	138	120
130	0.15	137	118

C. Variation of the Applied Current at Constant Mass Flow Rate

The effect on arcjet performance of varying the applied current to increase specific energy ($P/\dot{m}$) can be examined in detail by comparing simulation results from the three $\dot{m}$ = 0.1 g/s cases. Predicted voltages and current distributions for these cases are very similar. Physically, the distribution of current is controlled by the behavior of current passage through the outer gas layer, which is in turn governed by the heat diffusivity in that layer. Since the heat diffusivity is essentially the same for these three cases, the current patterns and voltages are nearly identical as well. The slightly negative V–I characteristic results primarily from higher electrical conductivity in the arc core due to the effect of increasing electron temperature with increasing current (Fig. 8). In addition, the arc width increases as the current is increased (Fig. 9), thus decreasing the width of the outer layer and making it easier for current to pass through to the wall.

The effects of arc widening and increasing temperature with increasing current result indirectly from the greater ohmic dissipation produced by higher current levels. This increased dissipation causes additional heating of the arc electrons, resulting in increased collisional energy transfer to the heavy species, thereby elevating gas temperatures. Higher electron temperatures also increase nonequilibrium dissociation and ionization rates and ambipolar diffusion, which cause the ionized region of the arc core to widen. Since the temperature increases and the arc core expands radially as the current is increased, the central region of high conductivity necessarily deepens and widens. The inlet pressure also increases with the applied current, rising from 1.13 atm at 60 A to 1.37 atm at 130 A for the mass flow rate of 0.1 g/s.

D. Variation of the Mass Flow Rate at Constant Specific Energy

The effect on arcjet performance of varying the mass flow rate can be isolated to some degree by comparing cases in Fig. 7 with different mass flow rates, but similar specific energies. Three of those cases have specific energies of 120 MJ/kg and specific impulses of approximately 1030 s. The main difference between these cases lies in their resulting current distributions (Fig. 10). Since increasing the mass flow rate increases the density, which directly decreases the heat diffusivity, the arc becomes more constricted. For a constant specific energy, this greater constriction produces higher electron and gas temperatures inside the arc and lower temperatures outside of the arc (Fig. 11). Since the width of the outer layer also increases with the mass flow rate, this leads to increased convection in the outer flow, and consequently, to a broader anode attachment zone (Fig. 10). This effect then translates into a higher predicted discharge voltage, from 89 V at 0.05 g/s to 137 V at 0.15 g/s.

The current and temperature distributions of these three cases look quite different, yet the specific impulse is nearly the same for each mass flow rate. Examination of the velocity and thrust distributions at the nozzle exit (Fig. 12) shows that this is due to the changing mass flow distributions over the channel cross section. While the exit velocity increases at all axial locations as the mass flow rate is increased at constant specific energy, the peak in momentum flux moves radially outward. Thus, more of the flow is actually farther from the centerline peak in velocity, resulting in a relatively unchanged overall specific impulse.

Examination of the distribution of energy in the exit flow for these three cases shows that as the mass flow rate is increased from 0.05 to 0.15 g/s, the fraction of energy in the axial kinetic mode increases from 34 to 44%. This occurs

because increasing the mass flow rate 1) increases the overall density, which tends to drive the flow toward equilibrium and 2) increases the propellant flow outside the arc, leaving a proportionally smaller amount of propellant in the core to be dissociated and ionized. The results of this mass flow variation study suggest that arcjet performance could be improved by increasing the operating pressure, which could be achieved by either reducing the constrictor diameter or increasing the mass flow rate at a constant specific energy.

V. Conclusions

A detailed, two fluid, viscous model has been developed to simulate the nonequilibrium gasdynamic flow in an electrothermal arcjet. Numerical results achieved with hydrogen propellant for calculated thrust, specific impulse, and discharge voltage compare well with experimental data from the University of Stuttgart radiation-cooled medium-power arcjet thruster. The internal two-dimensional structure of the flow is revealed, particularly with respect to arc development and anode attachment, and the two-temperature nature of the flow is evident. In particular, this model has shown that current passage between the highly ionized arc core and the anode wall can be explained by 1) elevated electron temperatures in the outer flow, which produce significant nonequilibrium dissociation and ionization and 2) ambipolar diffusion of ions and electrons from the arc core into the outer flow. It is the incorporation of a separate energy equation for the electrons, which previous arcjet models lacked, that allows this attachment process, and therefore, leads to better predictions of voltage and performance. In addition, the model of this research has been used to identify and explain performance trends observed by varying the applied current and mass flow rate. An important task for future research is the elimination of the requirement that the current must attach downstream of the constrictor exit. It is believed that a detailed analysis of the anode sheath layer may reveal boundary conditions that would allow unconstrained and physically consistent positioning of the anodic arc attachment.

Acknowledgment

This research was supported by a National Defense Science and Engineering Graduate Fellowship administered by the U.S. Army Research Office.

References

[1]Spurrett, R., and Bond, R. A., "Modelling Arcjet Thruster Performance," IEPC-91-110, Oct. 1991.

[2]Glocker, B., Schrade, H. O., and Sleziona, P. C., "Numerical Prediction of Arcjet Performance," AIAA Paper 90-2612, July 1990.

[3]Glocker, B., and Auweter-Kurtz, M., "Numerical and Experimental Constrictor Flow Analysis of a 10kW Thermal Arcjet," AIAA Paper 92-3835, July 1992.

[4]Martinez-Sanchez, M., and Sakamoto, A., "Simplified Analysis of Arcjet Thrusters," AIAA Paper 93-1904, June 1993.

[5]Andrenucci, M., Scortecci, F., Capecci, G., and Wünsch, T., "Development of a Computer Programme for the Analysis of Arcjet Nozzles," IEPC-91-113, Oct. 1991.

[6]Butler, G. W., and King, D. Q., "Single and Two Fluid Simulations of Arcjet Performance," AIAA Paper 92-3104, July 1992.

[7]Rhodes, R., and Keefer, D., "Modeling Arcjet Space Thrusters," AIAA Paper 91-1994, June 1991.

[8]Rhodes, R., and Keefer, D., "Comparison of Model Calculations with Experimental Data from Hydrogen Arcjets," IEPC-91-111, Oct. 1991.

[9]Miller, S. A., "Multifluid Nonequilibrium Simulation of Arcjet Thrusters," Sc.D. Dissertation, Massachusetts Inst. of Technology, Cambridge, MA, Feb. 1994.

[10]Sutton, G. W., and Sherman, A., *Engineering Magnetohydrodynamics*, McGraw–Hill, New York, 1965, Chap. 5.

[11]Biasca, R. J., *Chemical Kinetics of Scramjet Propulsion*, M.S. Thesis, Massachusetts Inst. of Technology, Cambridge, MA, Sept. 1988, Chap. 2.

[12]Rogers, R. C., and Schexnayder, C. J., "Chemical Kinetic Analysis of Hydrogen-Air Ignition and Reaction Times," NASA TP 1856, July 1981.

[13]Janev, R. K., Langer, W. D., Evans, K., and Post, D. E., *Elementary Processes in Hydrogen-Helium Plasmas*, Springer–Verlag, New York, 1987, Chaps. 2–4.

[14]Mitchner, M., and Kruger, C., *Partially Ionized Gases*, Wiley, New York, 1973, Chaps. 3–5.

[15]Sheppard, E. J., *Nonequilibrium Ionization in Electromagnetic Accelerators*, Ph.D. Dissertation, Massachusetts Inst. of Technology, Cambridge, MA, 1993, Chap. 3.

[16]Grier, N. T., "Calculation of Transport Properties of Ionizing Atomic Hydrogen," NASA TN D-3186, April 1966.

[17]Belov, V. A., "Viscosity of Partially Ionized Hydrogen," *High Temperature*, Vol. 5, No. 1, 1967, pp. 31–36.

[18]Vanderslice, J. T., Weissman, S., Mason, E. A., and Fallon, R. J., "High-Temperature Transport Properties of Dissociating Hydrogen," *Physics of Fluids*, Vol. 5, No. 2, 1962, pp. 155–164.

[19]Devoto, R. S., "Transport Coefficients of Partially Ionized Hydrogen," *Journal of Plasma Physics*, Vol. 2, Pt. 4, 1968, pp. 617–631.

[20]MacCormack, R. W., and Baldwin, B. S., "A Numerical Method for Solving the Navier-Stokes Equations with Application to Shock-Boundary Layer Interactions," AIAA Paper 75-1, Jan. 1975.

[21]Glocker, B., and Auweter-Kurtz, M., "Radiation Cooled Medium Power Arcjet Experiments and Thermal Analysis," AIAA Paper 92-3834, July 1992.

[22]Hoskins, W. A., Kull, A. E., and Butler, G. W., "Measurement of Population and Temperature Profiles in an Arcjet Plume," AIAA Paper 92-3240, July 1992.